Fusion of Target and Shadow Regions for Improved SAR ATR

Jae-Ho Choi, Myung-Jun Lee, Nam-Hoon Jeong, Geon Lee, and Kyung-Tae Kim, *Member, IEEE*

***Abstract*— Synthetic aperture radar (SAR) systems, which operate under a slant-viewing geometry, inevitably entail shadow regions in the resulting radar image. Such shadow profiles contain backprojected signatures of an object's configuration as with target profiles; however, they are rarely utilized in current SAR-based recognition techniques. A major challenge in leveraging shadow information together lies in the intrinsic limitation of current single-pathway approaches, in which the target and shadow cannot be addressed simultaneously because of their incompatible domain properties. Hence, we herein propose novel solutions that enable the successful fusion of target and shadow regions within SAR for the first time. First, we devise new image preprocessing techniques specifically customized for shadows to compensate for their unique domain characteristics, which are distinct from the target. Second, we introduce a parallelized SAR processing mechanism such that a network can independently extract features oriented toward each conflicting modality. Third, adaptive fusion strategies are proposed for the optimal integration of features from each region while considering their relative significance layer by layer. Extensive experiments on public benchmark datasets demonstrate that the proposed framework allows a network to effectively employ shadow signatures and targets, thereby outperforming previous methods significantly for all setups.**

***Index Terms*— Attention mechanism, automatic target recognition (ATR), feature-level fusion, information fusion of target and shadow (IFTS), synthetic aperture radar (SAR).**

I. Introduction

SYNTHETIC aperture radar (SAR) is an active imaging sensor characterized by its ability to generate high-resolution radar images in all-day, all-weather, and long-range conditions [1]. Its unique electromagnetic properties compared with optical imagery allow it to be leveraged as a key information source in various surveillance and reconnaissance systems [2]. However, on the other hand, its electromagnetic reflections also cause some complications, such as differences in the scattering mechanism, anisotropic factors, contamination from clutter or jamming signals, and speckle noise, resulting in less intuitive visual interpretations [3]–[8]. In this respect, the manual analysis from massive SAR image streams requires considerable human and material resources; this has consequently necessitated the development of SAR automatic target recognition (ATR) technologies.

Traditional SAR-ATR algorithms are primarily performed in three stages: detection, feature extraction, and classification [9]–[19]. Detection is a process of identifying only the regions of interest (ROI) from a wide SAR scene and can generally be achieved using constant false alarm rate-based adaptive thresholding techniques [20]. Subsequently, in the feature extraction stage, all the ROI templates are projected onto a lower dimensional latent space such that each of them can be well aligned with respect to the corresponding category. Finally, some data-driven classifiers, such as AdaBoost, random forest, and support vector machine, can be exploited to automatically specify the detailed class of the target.

Among them, the feature extraction phase is typically regarded as one of the most essential and intractable factors in determining the ATR performance [21], [22]. Accordingly, most traditional SAR-ATR studies have focused on the manual construction of salient features suitable for SAR imagery based on various signal processing algorithms, such as scattering center extraction [12], [13], advanced filtering [14], graphical modeling [15], image transformation [16], and compressed sensing [17]–[19]. These approaches have realized significant achievements but still retain clear drawbacks, i.e., their encoding pipelines are computationally inefficient; in particular, the improvement rate of recognition accuracy saturates gradually because of the intrinsic limitations of heuristics in handcrafted feature (HF) engineering.

The advent of deep learning (DL) frameworks in the pattern analysis field has enabled the automatic formation of optimal feature descriptors from arbitrary raw input data [23]–[26]. Inspired by this attractive property, a large body of studies have attempted for successful application of the DL framework to SAR-ATR [3], [27]–[39], yielding remarkable performance enhancements compared with previous HF-based approaches [9]–[19]. Despite a few methodological differences among these approaches, they share a common principle, i.e., to develop SAR-friendly DL-based algorithms by introducing an inductive bias associated with the unique domain characteristics of SAR imagery into the DL model. Chen *et al.* [3] proposed a parameter-efficient network architecture fully composed of convolutional modules to compensate for insufficient labeled SAR data. Moreover, in terms of input data for the network, SAR-specific data

Manuscript received February 27, 2022; accepted April 5, 2022. Date of publication April 8, 2022; date of current version April 25, 2022. This work was supported by the Energy Cloud Research and Development Program through the National Research Foundation of Korea (NRF) funded by the Ministry of Science, ICT under Grant NRF-2019M3F2A 1073402. *(Corresponding author: Kyung-Tae Kim.)*

Jae-Ho Choi, Nam-Hoon Jeong, Geon Lee, and Kyung-Tae Kim are with the Department of Electrical Engineering, Pohang University of Science and Technology, Pohang 790-784, South Korea (e-mail: jhchoi93@postech.ac.kr; sonata@postech.ac.kr; glee72@postech.ac.kr; kkt@postech.ac.kr).

Myung-Jun Lee is with the Mission Operation and Infrastructure Service Division, National Satellite Operation and Application Center, Korea Aerospace Research Institute, Daejeon 305-806, South Korea (e-mail: mjlee90@kari.re.kr).

Digital Object Identifier 10.1109/TGRS.2022.3165849

augmentation methods were presented using several image transformation techniques [27], [28] or generative adversarial networks [29], [30], while, in terms of network training, domain adaptation-based learning strategies were suggested for transferring semantic representations from large-size optical data to SAR [31]–[33]. To fully utilize the spatiotemporal properties of SAR sequences, convolutional neural network (CNN)–recurrent neural network (RNN) or 3-D CNN topologies were adopted in [34]–[36]. Meanwhile, to leverage the phase characteristics of SAR more effectively, Zhang *et al.* [37] introduced a complex CNN architecture. In recent years, to solve reliability issues arising from the mixed learning of clutter information within SAR training templates [38], [40], [41], novel SAR preprocessing schemes that enable the preremoval of clutter components have also been proposed [38], [39].

The studies above demonstrate the importance of inducing a network to better reflect SAR domain properties such that ATR tasks can be performed successfully instead of employing the typical DL algorithm developed for optical images as it is. Meanwhile, there also exists an additional domain characteristic of SAR that represents a distinct difference from other sensing modalities, i.e., the shadow information. Specifically, while electro-optical or infrared sensors form target images with a direct downward view, SAR signals are obtained from a slant transceiving path [42], [43], which inevitably yields relatively wide shadow areas in the resultant images [27], [44]. Such a shadow region in the SAR image contains backprojected profiles of the object configuration and, hence, can be utilized for ATR, as with a target region [45]–[50]. However, despite the useful information from the shadow domain, attempts to simultaneously use the target and shadow profiles for achieving further improvements in ATR performance are highly limited. To the best of our knowledge, with regard to the recent DL-based SAR-ATR approaches, the integration of the capability of the deep neural network (DNN) in automatic feature extraction with the information fusion of target and shadow (IFTS) has not been thoroughly investigated.

The difficulty in incorporating the DL framework into the IFTS is primarily attributable to the inherent nature of shadow areas, which is clearly different from that of the target images. First, as shown in Fig. 1, shadow regions in SAR typically represent significantly lower intensity levels compared with the target or clutter regions. In addition, unlike the target area, whose internal pixels are composed of positive scattering peaks, most of the shadow pixels are based on negative scattering peaks. Nevertheless, conventional DNN architectures are not suitable for extracting complementary feature representations from each region, considering the contradictory characteristics of the target and shadow, but rather are configurated to focus only on the target region. Consequently, semantic signatures from shadows are highly likely to be suppressed during the max-pool-based feature encoding in a general DNN model [51]. Second, the shadow area in an SAR image is highly sensitive to the variation in depression angles compared with the target area [27], [52]. Correspondingly, under practical conditions with significantly

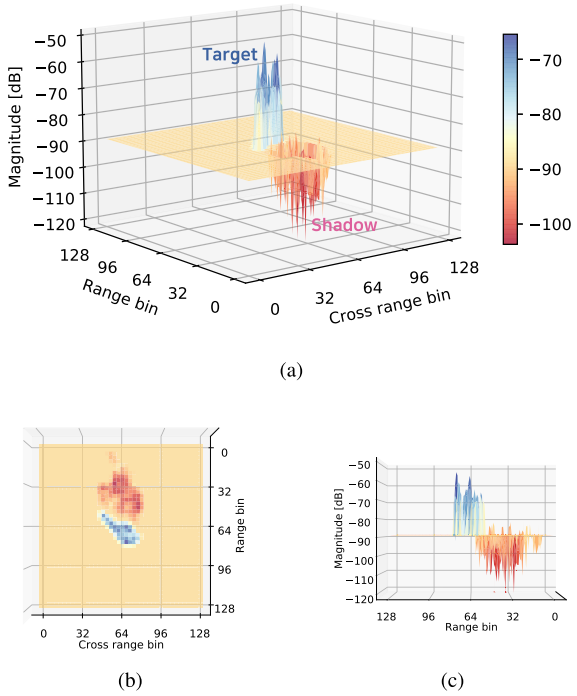

Fig. 1. Electromagnetic amplitude levels in SAR imagery. Target and shadow regions are marked in blue and red, respectively, and clutter pixels are excluded for visual clarity. (a) 3-D view. (b) Top view. (c) Side view.

different depression angles between the training and test SAR data, the shadow information may not be beneficial at all; in fact, it may deteriorate the ATR performance.

Considering the aforementioned problems, unlike typical DL-based SAR-ATR approaches, which focus only on extracting salient features from target areas, we propose a novel framework that can achieve a successful IFTS through a parallelized processing scheme and adaptive multistage feature fusion, thereby affording further improved ATR performance. The main contributions of this study are threefold as follows.

1) A major problem in current DL-based SAR-ATR methods is their incapability in performing independent processing specialized for each domain modality of targets and shadows since their structural limitations cause each region to undergo uniform preprocessing and feature encoding. To tackle this problem, we propose a novel parallelized SAR processing pipeline, in which target and shadow areas are first segmented from an input SAR image, followed by parallel preprocessing and DNN-based feature encoding specifically customized for each region. Subsequently, the deep representations extracted from each region are fused to produce a single final decision. Consequently, domain-centric processing of target and shadow from a single image can be realized; in particular, the utility of shadow information can be improved significantly, even under situations involving variable depression angles.
2) The target and shadow regions in an SAR template contain overlapping information and contribute differently

TABLE I
ATR PERFORMANCE (TEST ACCURACY, %) BASED ON SEVERAL REGIONAL COMBINATIONS OF PARTIALLY SEGMENTED SAR IMAGES UNDER SOC AND EOC-1 SETUPS

	SOC (Training: 17, Test: 15, 10 class)			**EOC-1 (Training: 17, Test: 30, 4 class)**		
	Target + Shadow	Target Only	Shadow Only	Target + Shadow	Target Only	Shadow Only
AConvNet [3]	96.15%	95.12%	79.58%	91.67%	91.83%	36.24%
LM-BN-CNN [38]	97.11%	96.30%	80.24%	93.54%	93.41%	39.22%
ESENet [39]	97.08%	96.69%	80.58%	93.03%	93.57%	38.67%
Average	96.78%	96.04%	80.13%	92.75%	92.94%	38.04%

from the perspective of ATR. In this respect, general feature fusion strategies [53], [54], such as lateral concatenation and elementwise sum, are not feasible for accommodating such information imbalances. Hence, we implement a novel domain fusion module (DFM), which induces the network to assign an adaptive weight in accordance with the influence of each region, thereby yielding complementary fusion. Moreover, a multistage fusion scheme is introduced to further improve the representation power of the fused feature.

3) It is noteworthy that the proposed IFTS framework is generic, so it can easily be combined with other DL-based SAR-ATR techniques to strengthen their perception ability in the shadow region. Based on this flexibility, we investigate the performance gain by applying the proposed IFTS framework to various baseline DNN backbones, developed for image classification and SAR-ATR; the results confirm that our framework can activate each network to incorporate shadow information successfully and provide more precise recognition under both standard operation conditions (SOCs) and extended operation conditions (EOCs). To the best of our knowledge, this is the first study to report the efficacy of the IFTS for both SOCs and EOCs based on the DL approach.

The remainder of this article is organized as follows. In Section II, the effects of shadows in the current DL-based SAR-ATR techniques are investigated from various perspectives. Subsequently, we discuss the necessity of parallelized processing pipelines customized for targets and shadows separately. In Section III, the methodology of the proposed IFTS framework is described in detail. Section IV presents the experimental results under various conditions using a public moving and stationary target acquisition and recognition (MSTAR) dataset [52] to validate the effectiveness of the proposed method. Finally, concluding remarks are provided in Section V.

II. MOTIVATION

In this section, the intrinsic incompatibility of current DL-based SAR-ATR approaches in addressing SAR shadow content is experimentally demonstrated. Subsequently, we explore the solutions for a successful IFTS.

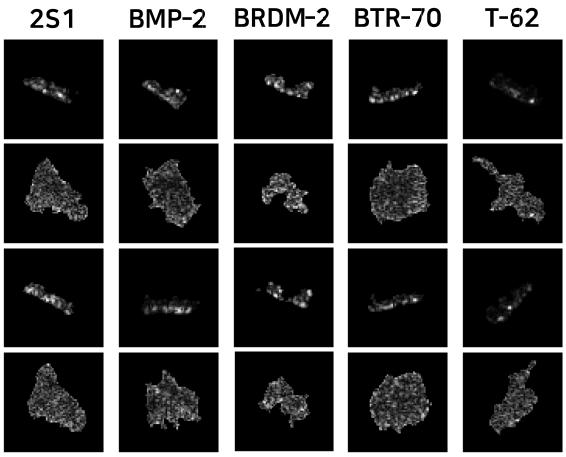

Fig. 2. Several SAR templates that are misclassified based on target regions but correctly classified based only on shadow regions. The first and third rows of the figure represent the target area of each SAR sample, and the second and fourth rows represent the corresponding shadow area.

A. Efficacy of Shadow Modality in SAR-ATR

First, to verify the discriminative potential of shadow (compared with the target area) in ATR, we measured the recognition accuracies with respect to regional combinations of partially segmented MSTAR SAR images (i.e., Target + Shadow, Target Only, or Shadow Only). In the experiments, we employed several backbone networks that were specifically designed for SAR, i.e., A-ConvNet [3], LM-BN-CNN [38], and ESENet [39], and the results are summarized in Table I. From the results under the ideal SOC, it can be observed that utilizing the shadow region alone even enables the networks to attain a stable ATR performance of approximately 80%, indicating that the shadow modality clearly contains some back-projected signatures for the objects of interest.

Based on the results, we perform an in-depth analysis on specific SAR templates where the network fails to recognize their classes based only on the target areas while achieving successful ATR even based on the shadow areas. Specifically, using the ESENet under the SOC setup, we investigate the cases that overlap with the 2581 SAR templates that are correctly classified based only on the shadow regions (the third row and third column result of Table I), among the 106 SAR templates that are misclassified based on the target regions (the third row and second column result of Table I). It is remarkable that a total of 68 SAR templates, 64.15% out

of the 106 failures on target, are found to belong to such cases, implying that the shadow has enough potentiality to provide complementary features compared with the target area. For more qualitative analysis, Fig. 2 shows several examples belonging to the aforementioned cases (i.e., cases that are misclassified based on target but correctly classified based on shadow). From the target images, it can clearly be recognized that the configuration details of each object are projected in one direction at a certain azimuth angle, making it almost impossible to provide discriminative information (i.e., maintaining quasi-rectangular contours even though they are reflected from different vehicles). On the other hand, corresponding shadow contours rather provide unique signatures representative of each vehicle.

Comparing the classwise shadow regions in Fig. 2, it can be observed that the shadow reflects the discriminative information of each vehicle in terms of the shape and size of its contour. On the one hand, in terms of shape, the shadow is fundamentally formed along with the point where the radar beam does not reach the object [55], and such a domain property of shadow enables its contour to involve the backscattered shape of the object [44], [45], as shown in the shadow profiles of T-62, which is able to reflect the main barrel of a tank. On the other hand, in terms of size, the shadow area in the SAR projection plane is essentially generated in proportion to the height of an object and inverse proportion to $\sin(\varepsilon)$, where ε denotes the depression angle between an SAR platform and an object of interest [27]. Namely, assuming that the depression angle variations between the training and test can properly be corrected (we address it in Section III-B), the shadow region becomes capable of indirectly reflecting the height information of the object that the target region cannot provide.

B. Necessity for Considering Shadow-Centric Processing in SAR-ATR

Belloni *et al.* [51] designed an evaluation protocol to numerically confirm the global contribution of the target, shadow, and clutter regions for DL-based ATR. By training a baseline CNN with partially segmented SAR regions, classification scores were observed for all possible combinations. Their experimental results notably indicated that the effect of utilizing both the target and shadow regions is insignificant in terms of ATR compared to utilizing only the target region, despite the discriminative/representative potentiality of shadow modality as discussed above, implying that a CNN is incapable of appropriately leveraging semantic representations from the shadow.

This undesirable phenomenon is due to the general CNN architectures centered solely on the feature extraction of the target, not the shadow. In other words, even though the shadow areas retain unique domain characteristics, which are exactly opposite to the target as discussed before (i.e., maintaining significantly lower intensity levels compared with the target or clutter and comprising pixels with negative local peaks), the structural nature of the CNN causes final features to be extracted based on pixels with higher intensity levels and positive local peaks. Eventually, as shown by the experimental results in [51], a typical CNN is likely to concentrate only on a target region, thereby causing the loss of useful discriminatory information within a shadow.

It is noteworthy that the effect of shadows on ATR becomes further aggravated under EOCs, where the depression angle during the test session varies considerably compared with the training data. As illustrated in Fig. 3, an SAR system projects each object onto a slant image projection plane spanned by the radar line of sight (RLOS). During slant projection, a geometric distortion in the form of a scale transformation is inevitably incurred across the resulting SAR imagery. The problem is that the degree of such image distortion differs between the target and shadow regions, even within a single SAR image reflected from the same object [27]. Formally, considering the spatial geometry, the target region in the SAR projection plane is scaled with a factor of $\cos(\varepsilon)$ into the range direction, whereas the shadow is scaled with a relatively large factor of $1/\sin(\varepsilon)$ [27], [52]. For example, under the condition of EOC-1 in an MSTAR dataset, where the training and test data are constructed based on depression angles of 17° and 30° (a detailed description of the dataset is provided in Section IV-A), respectively, the relative scaling ratio of the target region within the test SAR template is computed as follows:

$$\frac{\cos(\varepsilon_{\text{test}})}{\cos(\varepsilon_{\text{train}})} = \frac{\cos 30^\circ}{\cos 17^\circ} \approx 0.91 \tag{1}$$

where $\varepsilon_{\text{train}}$ and $\varepsilon_{\text{test}}$ represent the depression angles in the training and test data, respectively. By contrast, a much greater degree of compression is generated in the shadow region as follows:

$$\frac{1/\sin(\varepsilon_{\text{test}})}{1/\sin(\varepsilon_{\text{train}})} = \frac{\sin 17^\circ}{\sin 30^\circ} \approx 0.58. \tag{2}$$

Fig. 4 shows the contours of the target and shadow on the SAR images captured from the same object at different depression angles (i.e., 15°, 17°, and 30°). As expected, unlike the target areas outlined with blue lines, which represents almost similar configurations irrespective of the depression angle, the shadow areas with pink lines undergo severe image variation as the depression angle of the SAR platform changes.

It is noteworthy that our experiments summarized in Table I also reflect the above discussions in a numerical manner. Despite the semantic potentiality of shadows, the comparison between the case involving both a segmented target and shadow and the case involving the target alone indicates only a slight performance improvement of 0.74% on average. Especially under a more practical condition (EOC-1), it is remarkable that all network configurations suffer from severe performance degradation when trained and inferenced with only shadows (i.e., exhibiting a level of accuracy with a slight difference from that of simply randomized outputs in the EOC-1's four-class classification task). This implies that the networks cannot extract any informative indicators from the shadow, particularly when different depression angles are involved between training and testing. Accordingly, DNNs based on both target and shadow information cannot benefit from the shadow; in fact, they yield rather degraded ATR performance compared with those based on the Target Only.

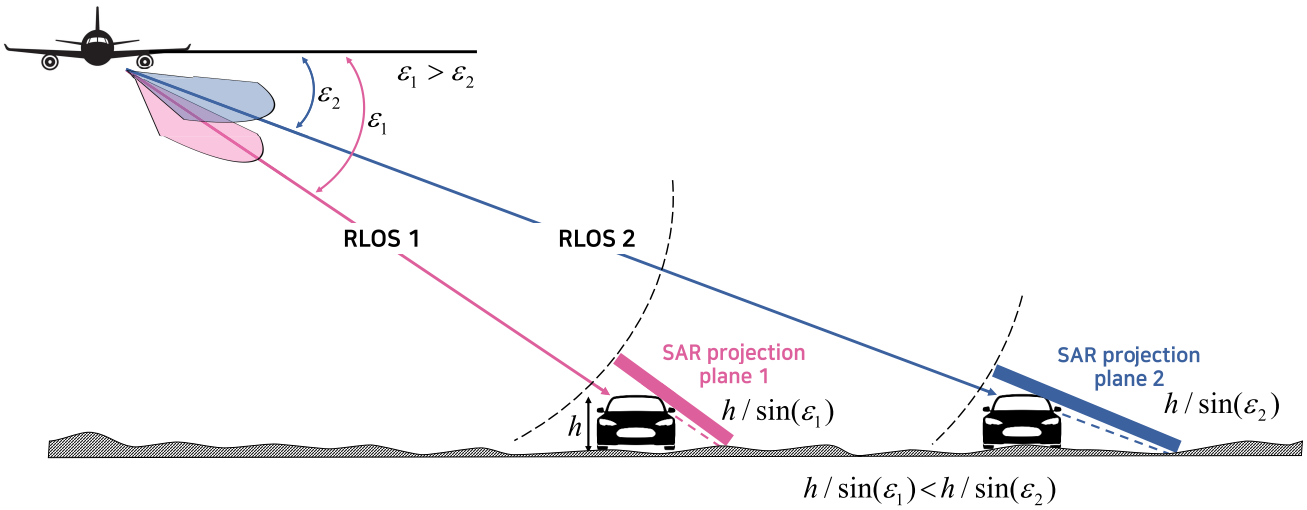

Fig. 3. Conceptual figure of SAR imaging system for different RLOS conditions (i.e., different depression angles).

The results shown in Table I explicitly demonstrate that the current approaches cannot combine the shadow information in a proper manner, and they depend only on the target information for SAR-ATR. For a successful IFTS, a network must be able to capture the unique domain characteristics of shadows and compensate for the regionwise scaling distortion with respect to the variation in the depression angle; this implies that shadow-centric processing must be accompanied together in the overall SAR-ATR mechanism in addition to the target area.

C. Necessity for Parallelized Processing Pipeline

In addition to the necessity for designing separate processing for SAR shadow, a fundamental bottleneck exists when combining shadow-centric processing with conventional DL-based ATR algorithms. Because the target and shadow regions are entangled within a single SAR template, independent processing optimized specifically for each modality is not feasible for implementation. In other words, when shadow-centric processing is applied to a specified SAR, the target area in the image will also be affected and vice versa.

Essentially, this problem is attributable to the single-pathway-based pipeline of current ATR approaches, in which uniform preprocessing and deep feature encoding are applied based on a specified SAR input, as shown in Fig. 5(a). In this regard, parallelized processing pipelines for the target and shadow must be established to manage the problem and realize independent processing oriented toward each modality. To this end, we herein propose a novel SAR-IFTS framework that enables parallelized pipelines by regarding target and shadow regions within a single SAR as unique modalities. Specifically, the entangled target and shadow regions from the input SAR image are separated first using image segmentation techniques, followed by independent processing suitable for each domain. Subsequently, the information pairs from the separated target and shadow are combined at a certain point to obtain a final single decision via a multimodal fusion scheme [56].

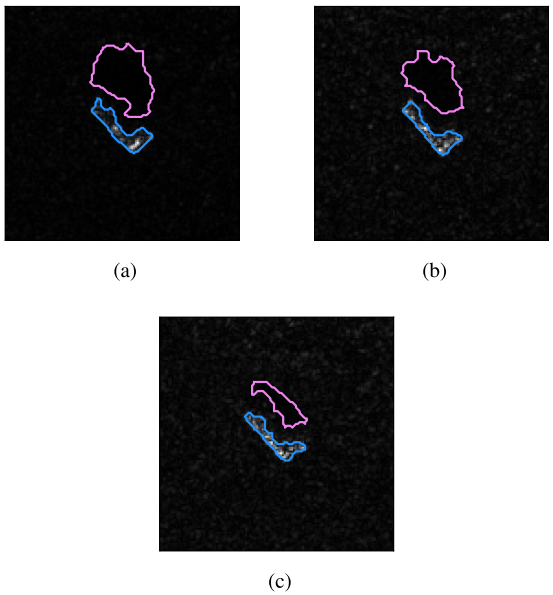

Fig. 4. Example SAR templates for 2S1 vehicle at same azimuth angle but different depression angles. Target and shadow regions in each image are indicated with blue and red contours, respectively. Depression angles of (a) 15°, (b) 17°, and (c) 30°.

As shown in Fig. 5(b)–(d), the typical multimodal fusion algorithms can be categorized into three primary schemes based on the type of information to be combined: pixel-, feature-, and decision-level fusions. Among them, feature-level fusion [see Fig. 5(c)] is expected to be the most suitable for performing the IFTS task since pixel-level fusion [see Fig. 5(b)] inevitably demands a sophisticated mechanism of integrating pixelwise information pairs with high dimensionality, and decision-level fusion [see Fig. 5(d)] cannot readily consider hierarchical inter-relationships between the two modalities.

Hence, a parallel processing pipeline coupled with a feature-level fusion scheme is adopted in the proposed ATR framework to facilitate independent processing customized for

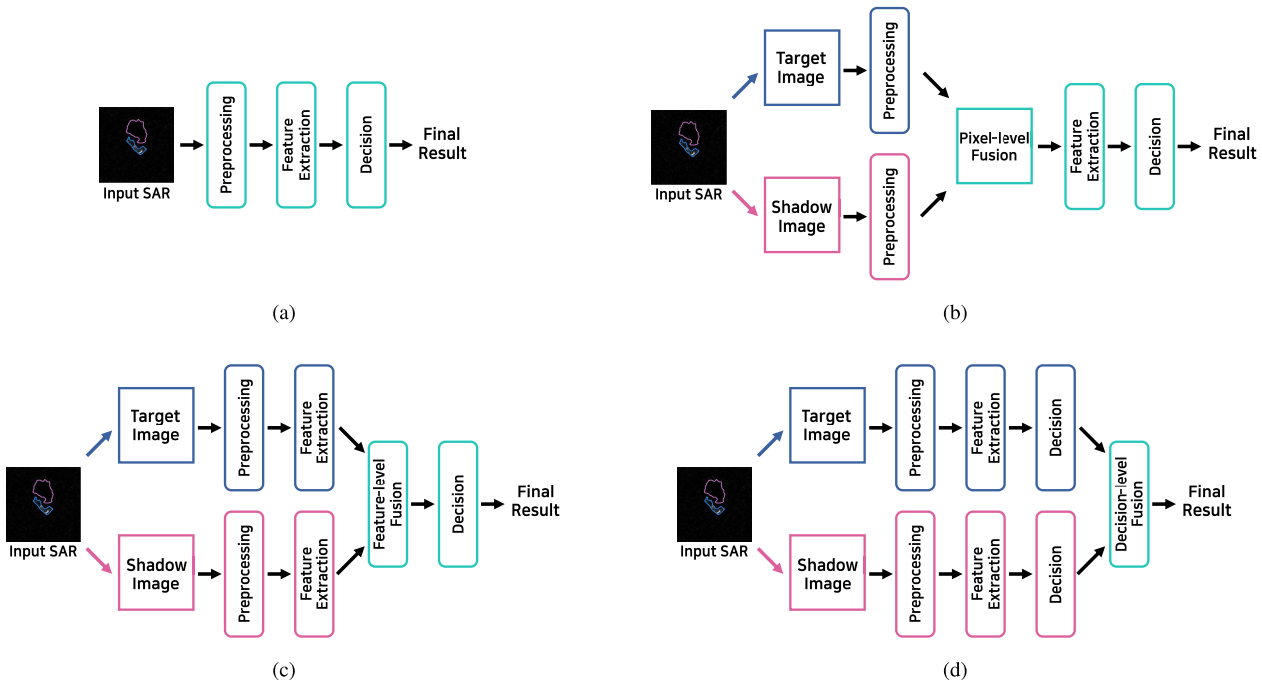

Fig. 5. Plausible approaches for realizing IFTS-based SAR ATR. (a) Conventional single-pathway-encoding pipeline. (b) Pixel-level fusion-based IFTS. (c) Feature-level fusion-based IFTS. (d) Decision-level fusion-based IFTS.

the target and shadow, separately, while ensuring full benefits from multimodal fusion. In particular, the fusion is based on a newly developed DFM operation, which allows a network to extract complementary representations while considering the priority of each modality. In Section III, we present the methodology of the proposed framework in detail.

III. Methodology

The overall concept of the proposed SAR-IFTS framework is presented in Fig. 6. As shown in the figure, the proposed framework first segments the target and shadow from a single SAR template, followed by image preprocessing and feature embedding specifically tailored for each region. Meanwhile, the representation pairs of the target and shadow extracted independently of the parallelized pipelines are combined based on novel feature fusion strategies to derive a single final decision. In this section, the stepwise procedures of the proposed framework are described in detail.

A. Segmentation of Target and Shadow Regions

Since an SAR image generally shows a mixture of backscattering reflections from the target, shadow, and clutter, separation of each component must be preceded to realize a parallel processing mechanism. Because the target is clustered in the high-intensity range, while the shadow is in the low-intensity range across the global SAR distribution, they can be separated using a series of image processing techniques, such as intensity-based binarization and morphological refinement. Inspired by the key idea presented in [16], [38], [57], and [58], we reestablished an SAR segmentation algorithm aimed at separating target and shadow regions from a single SAR image.

Let an SAR image template be denoted as $I[m, n]$ with $1 \leq m \leq M$ and $1 \leq n \leq N$, where (m, n) are the coordinates on the down- and cross-range dimensions, respectively. Because radar reflection represents different levels of electromagnetic intensity depending on its RLOS range between the mounting platform and targets of interest, the intensity variation in the SAR image must first be adjusted

$$I_v[m, n] = \frac{I[m, n]}{\sum_{m=1}^{M} \sum_{n=1}^{N} I[m, n]} \quad \forall (m, n). \tag{3}$$

Based on the adjusted SAR template $I_v[m, n] \in \mathbb{R}^{M \times N}$, the target and shadow regions can be segmented via the following procedures.

Step 1: Select only pixels that correspond to the upper 3% intensity from the entire histogram of $I_v[m, n]$ to generate a binarized target mask (i.e., 1 for the target and 0 for the remainder). Likewise, select only the pixels with the lower 25% amplitude to create a corresponding binary shadow mask.

Step 2: Perform counting filtering for each mask such that spurious pixels can be suppressed to the maximum extent.

Step 3: Morphological closing is applied to bind the areas of interest and smooth the edge components.

Step 4: Obtain the final refined binary mask by extracting only the max-connected region.

Step 5: Multiply each binary mask with $I_v[m, n]$ to segment the target and shadow pixels. Subsequently, obtain the final target image $T[p, q] \in \mathbb{R}^{P \times Q}$ and shadow image $S[p, q] \in \mathbb{R}^{P \times Q}$ by cropping a rectangular area with a width of P and a height of Q around the center of mass from each region.

To provide a clear illustration, Fig. 7 shows the stepwise outputs of the proposed target/shadow segmentation process based on the SAR image chip of a T-72 tank. It is noticed that the target and shadow regions can be roughly be separated through hard thresholding [see Fig. 7(b) and 7(h)]

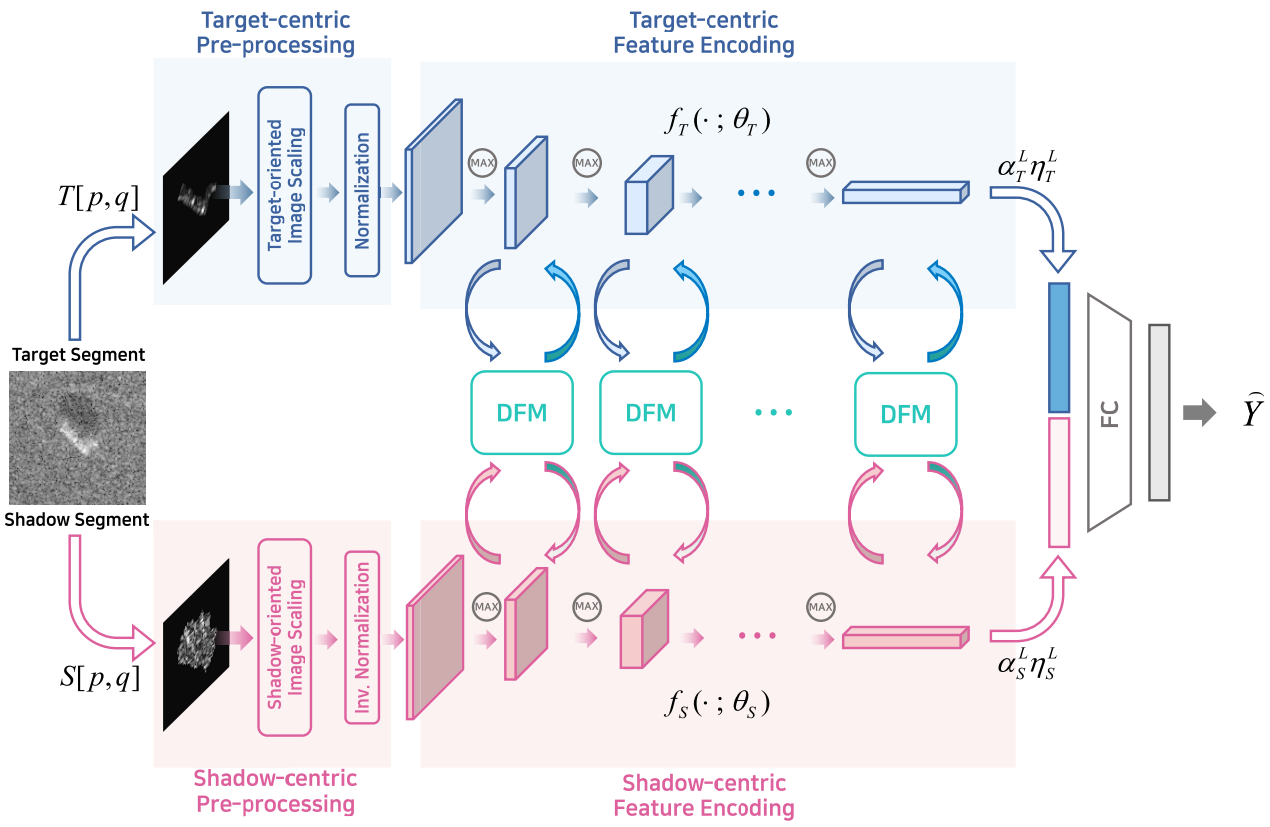

Fig. 6. Overall pipeline of the proposed SAR IFTS framework.

from $I_v[m,n]$ and then gradually refined by counting filtering [see Fig. 7(c) and 7(i)] and morphological adjustments [see Fig. 7(d) and 7(j)]. Finally, the segmented images for target $T[p,q]$ and shadow $S[p,q]$ can be obtained by multiplying each binary mask with $I_v[m,n]$ in an element-wise manner and readjusting the center points, as shown in [see Fig. 7(j) and 7(i)], respectively.

B. Parallel Processing Customized for Target and Shadow Regions

The core of the proposed SAR-ATR framework lies in the novel concept of the parallelized processing mechanism (see Fig. 6), which can structurally ensure independent processing for $T[p,q]$ and $S[p,q]$ by regarding each of them as a disparate input modality. This, in turn, enables flexible implementation of the preprocessing and feature embedding pipelines customized for each modality while accounting for their characteristic differences. It is noteworthy that the target and shadow show distinct characteristic differences in two major aspects, as mentioned in Section II-B: 1) in cases where the depression angle between the training and test conditions fluctuates, each region undergoes different degrees of image distortion in the form of scale transformation and 2) when approaching the electromagnetic scattering centers of an object, the reflected amplitude levels in the target region tend to increase, whereas the amplitudes of the shadow region gradually decrease. The two domain discrepancies are first compensated using our parallelized preprocessing techniques.

1) Preprocessing for Target and Shadow Regions: Recall that the target and shadow images are scaled across the down range dimension with a factor of $\cos(\varepsilon)$ and $1/\sin(\varepsilon)$, respectively, with respect to the depression angle ε between an SAR platform and an object of interest. Hence, when geometrical adjustment is performed based on the target area, the shadow area would undergo another form of scaling distortion as well and vice versa. Now that the independent processing of the target and shadow is guaranteed by the parallelized mechanism, we can mitigate the scaling distortion of both $T[p,q]$ and $S[p,q]$ using the regionwise scaling factor. To this end, we adopt a general affine transformation technique. Let the depression angle $\varepsilon_{\text{test}}$ in the test environment be changed from the training depression angle $\varepsilon_{\text{train}}$ (i.e., $\varepsilon_{\text{test}} \neq \varepsilon_{\text{train}}$). Then, for the testing conditions, we transform $T[p,q]$ and $S[p,q]$ in the (p,q) Cartesian coordinates to $T_c[p',q']$ and $S_c[p',q']$ in the rescaled (p',q') Cartesian coordinates, respectively, where the (p,q) and (p',q') coordinates are correlated as follows [27]:

$$\begin{pmatrix} p' \\ q' \end{pmatrix} = \begin{pmatrix} \lambda & 0 \\ 0 & 1 \end{pmatrix} \begin{pmatrix} p \\ q \end{pmatrix} \tag{4}$$

where λ denotes the recalibrating parameter, which is obtained by the inverse of the scaling distortion within each test region

$$\lambda = \begin{cases} \dfrac{\cos(\varepsilon_{\text{train}})}{\cos(\varepsilon_{\text{test}})}, & \text{for target} \\ \dfrac{1/\sin(\varepsilon_{\text{train}})}{1/\sin(\varepsilon_{\text{test}})}, & \text{for shadow.} \end{cases} \tag{5}$$

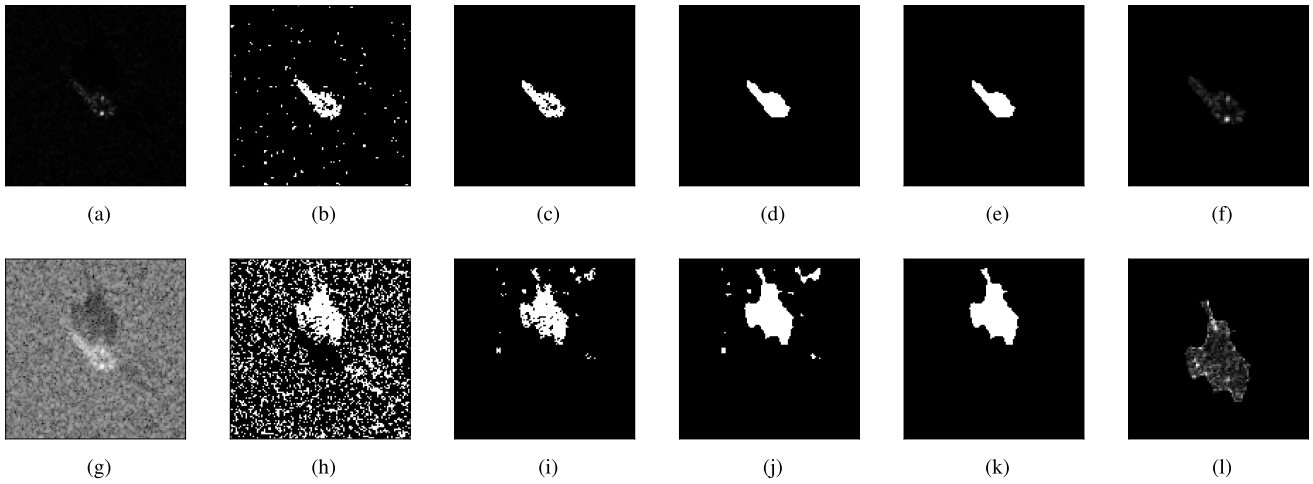

Fig. 7. Stepwise output examples of the proposed segmentation technique for the SAR template. (a) Original SAR image for T-72 tank in the linear scale. (b) Target mask after upper thresholding. (c) Target mask after counting filtering. (d) Target mask after morphology. (e) Refined target mask obtained by selecting only the max-connected region. (f) Final segmented target image. (g) Original SAR image for T-72 tank in the log scale. (h) Shadow mask after lower thresholding. (i) Shadow mask after counting filtering. (j) Shadow mask after morphology. (k) Refined shadow mask obtained by selecting only the max-connected region. (l) Final segmented shadow image.

In summary, in the proposed IFTS framework, the input pair of segmented images $T[p,q]$ and $S[p,q]$ are used without modification for the training phase, and the rescaling transformation in (4) is additionally applied for the test phase such that even the test input pairs under $\varepsilon_{\text{test}}$ become consistent with the training depression angle $\varepsilon_{\text{train}}$.

Next, in terms of image intensity, we compensate for the conflicting domain characteristics of the target and shadow through regionwise normalization, ensuring consistent statistical distributions and appropriate dynamic range levels corresponding to each region. Similar to the regionwise rescaling, normalization is also performed in a parallelized manner to readily manage the unique distribution of each modality. For example, $T_c[p',q']$ and $S_c[p',q']$ in the test phase are normalized as follows:

$$T_n\big[p',q'\big] = \begin{cases} \dfrac{T_c\big[p',q'\big]-\mu_T}{\sigma_T}, & \forall\big(p',q'\big)\in\mathbb{I}_T \\ \min\limits_{p',q'}\left\{\dfrac{T_c\big[p',q'\big]-\mu_T}{\sigma_T}\right\}, & \forall\big(p',q'\big)\notin\mathbb{I}_T \end{cases} \tag{6}$$

$$S_n\big[p',q'\big] = \begin{cases} -\dfrac{S_c\big[p',q'\big]-\mu_S}{\sigma_S}, & \forall\big(p',q'\big)\in\mathbb{I}_S \\ \min_{p',q'}\left\{-\dfrac{S_c\big[p',q'\big]-\mu_S}{\sigma_S}\right\}, & \forall\big(p',q'\big)\notin\mathbb{I}_S \end{cases} \tag{7}$$

where

$$\mathbb{I}_T = \big\{\big(p',q'\big)\mid T_c\big[p',q'\big]\neq 0\big\}$$
$$\mathbb{I}_S = \big\{\big(p',q'\big)\mid S_c\big[p',q'\big]\neq 0\big\}.$$

Here, given that $T_c[p',q']$ and $S_c[p',q']$ inevitably include lots of zero-point pixels and consequential discontinuities around the contours due to the previous segmentation process, we exclude such zero points during the regionwise normalization (i.e., considering only the nonzero pixels $\mathbb{I}_T$ and $\mathbb{I}_S$ for target and shadow) and replace the zero-point pixels with a minimum magnitude of the normalized images. $T_n[p',q']\in\mathbb{R}^{P\times Q}$ and $S_n[p',q']\in\mathbb{R}^{P\times Q}$ represent the final preprocessed images for the target and shadow, respectively. In addition, μ_T and μ_S denote the sample means of the SAR images in the target and shadow regions, respectively; σ_T and σ_S denote sample variances for the corresponding regions, respectively. Note that the normalized output of the shadow is reversed considering its inverse characteristics, as shown in Fig. 1 (we refer to it as "inverse normalization" hereinafter); as such, consistent with the target image, the negative peaks of $S_c[p',q']$ can be converted into positive peaks.

2) DNN-Based Feature Encoding for Target and Shadow Regions: Considering that the preprocessed images $T_n[p',q']$ and $S_n[p',q']$ separately involve the signatures of the object of interest, a deep CNN model can be utilized for automatic extraction of the complementary representation from each modality. In this subsection, we formulate a detailed methodology to extract a domain-specific feature representation based on each preprocessed image, given an arbitrary CNN model.

A general CNN architecture is configured to iterate the nonlinear embedding and downsampling operations through the hierarchical combinations of convolutional mapping and pooling modules, thereby effectively deriving the global and local features from a high-dimensional input [59]. By unifying various combinations of internal network modules and their hierarchical connections, numerous CNN topologies can be constructed.

In this study, we do not focus on the topology of the deep network itself. Instead, we attempt to identify a method to convert a specified CNN-based feature extractor into an extended model aimed at the IFTS task. Let $f(\cdot\,;\theta)$ denote a CNN-based extractor with internal parameters θ, which is designed to project an arbitrary input image $A\in\mathbb{R}^{P\times Q}$ into the latent space $f(A\,;\theta)=\{\eta^1,\eta^2,\ldots,\eta^L\}$, where η^l represents the feature from the lth encoding layer. Then, we duplicate it for extension to the parallelized encoding pair $f_T(\cdot\,;\theta_T)$ and $f_S(\cdot\,;\theta_S)$, which exhibits an identical network

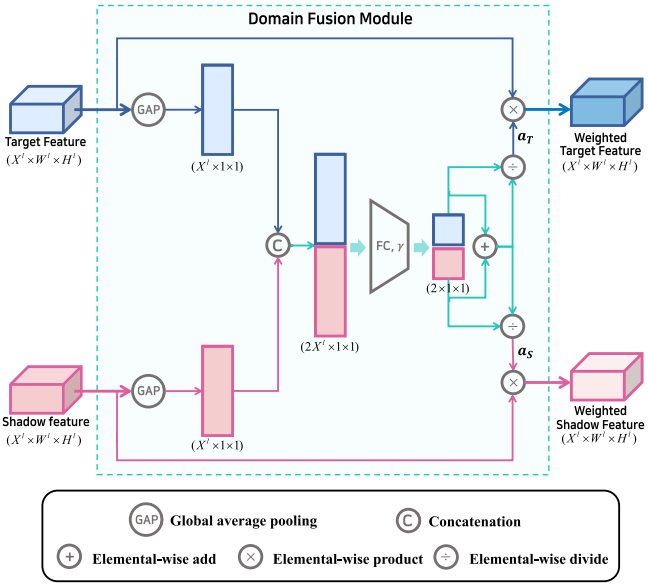

Fig. 8. Detailed workflow of DFM.

topology with $f(\cdot\,;\theta)$ but different internal parameters such that each pathway (or subnetwork) can be organized to address the multimodal input pair T_n and S_n, respectively (see Fig. 6). Specifically, for a set of SAR images $\mathcal{I}$, an SAR template $I[m,n] \sim \mathcal{I}$ uniformly sampled from $\mathcal{I}$, and two preprocessed regionwise images $T_n \sim \mathcal{T}$ and $S_n \sim \mathcal{S}$, the parallelized encoding pipelines of $f_T(\cdot\,;\theta_T)$ and $f_S(\cdot\,;\theta_S)$ allow each subnetwork to be individually optimized from $\mathcal{T}$ and $\mathcal{S}$, thereby yielding the feedforward generation of regionwise feature pairs $f_T(T_n;\theta_T) = \{\eta_T^1, \eta_T^2, \ldots, \eta_T^L\}$ (for target) and $f_S(S_n;\theta_S) = \{\eta_S^1, \eta_S^2, \ldots, \eta_S^L\}$ (for shadow).

It is noteworthy that our pipeline enables a network to extract features specifically oriented toward each conflicting region, but, on the other hand, there remains an additional issue of how to properly combine the representation pairs from the target and shadow to derive a single final decision. In the next subsection, we introduce novel fusion strategies for the target and shadow, including the DFM and the multistage fusion scheme.

3) Adaptive Fusion of Target and Shadow Features: In SAR imagery, the target and shadow regions have imbalanced significance for ATR. Namely, despite the usefulness of shadows, they definitely retain a lower level of content information than the target areas. In this respect, the regionwise features η_T and η_S must be adaptively incorporated with unequal weight ratios.

Instead of determining the weight for each modality empirically, we allow the network to assign adaptive weights on its own through a novel DFM. As illustrated in Fig. 8, the DFM is configured to take the feature pair of a certain layer $\{\eta_T^l, \eta_S^l\}$ as the input and then compute the corresponding weight ratio $\{\alpha_T^l, \alpha_S^l\}$ using the attention mechanism [60], [61], which enables the automatic update of concentration weights from the input features. Specifically, the 3-D input features $\eta_T^l \in \mathbb{R}^{X^l \times W^l \times H^l}$ and $\eta_S^l \in \mathbb{R}^{X^l \times W^l \times H^l}$ are compressed first

Algorithm 1 Main Learning Algorithm of the Proposed SAR IFTS Framework

Input:
training SAR samples $\mathcal{I} = \{I^{(1)}, I^{(2)}, \ldots, I^{(K)}\}$,
corresponding label $\mathcal{Y} = \{Y^{(1)}, Y^{(2)}, \ldots, Y^{(K)}\}$,
batch size B, network structure f.
Step one: Image segmentation & preprocessing
for $I^{(k)}[m,n] \in \mathcal{I}$ **do**
  for all $k \in \{1, \ldots, K\}$ **do**
    Compute $I_v^{(k)}[m,n]$ by (3).
    Segment target $T^{(k)}[p,q]$ and shadow $S^{(k)}[p,q]$ from $I_v^{(k)}[m,n]$ as in Section III-A.
    Compute $T_n^{(k)}[p,q]$ by (6). ▷ *Normalization*
    Compute $S_n^{(k)}[p,q]$ by (7). ▷ *Inv. normalization*
  end for
end for
return target samples $\mathcal{T} = \{T_n^{(1)}, T_n^{(2)}, \ldots, T_n^{(K)}\}$ and shadow samples $\mathcal{S} = \{S_n^{(1)}, S_n^{(2)}, \ldots, S_n^{(K)}\}$.
Step two: Network training
Construct f_F, composed of $f_T(\cdot\,;\theta_T)$, $f_S(\cdot\,;\theta_S)$, and DFMs, referring to the given structure f.
Initialize θ_T, θ_S, θ_F.
for sampled minibatch $\mathcal{B} \subset \{1, \ldots, K\}$, $\{T_n^{(b)}\} \subset \mathcal{T}$, $\{S_n^{(b)}\} \subset \mathcal{S}$, $\{Y^{(b)}\} \subset \mathcal{Y}$ **do**
  for all $b \in \mathcal{B}$ **do**
    $P(\tilde{y} \mid T_n^{(b)}, S_n^{(b)}) = f_F(T_n^{(b)}, S_n^{(b)}\,;\theta_T, \theta_S, \theta_F)$. ▷ *Parallel encoding*
  end for
  $\mathcal{L} = -\frac{1}{B}\sum_{b\in\mathcal{B}} \log P(\tilde{y} = Y^{(b)} \mid T_n^{(b)}, S_n^{(b)})$.
  $(\theta_T^*, \theta_S^*, \theta_F^*) = \text{argmin}_{\theta_T,\theta_S,\theta_F} \mathcal{L}$.
end for
return trained network $f_F(\cdot\,;\theta_T^*, \theta_S^*, \theta_F^*)$.

via a global average pooling operation to form 1-D vectors $\mathbf{z}_T^l \in \mathbb{R}^{X^l}$ and $\mathbf{z}_S^l \in \mathbb{R}^{X^l}$

$$\{\mathbf{z}_T^l\}_x = \frac{1}{W^l \times H^l} \sum_{i=1}^{H^l} \sum_{j=1}^{W^l} \eta_T^l[x,i,j] \tag{8}$$

$$\{\mathbf{z}_S^l\}_x = \frac{1}{W^l \times H^l} \sum_{i=1}^{H^l} \sum_{j=1}^{W^l} \eta_S^l[x,i,j] \tag{9}$$

where $\{\cdot\}_x$ denotes the xth element of the compressed feature vector. By concatenating $\mathbf{z}_T^l$ and $\mathbf{z}_S^l$ to form $\mathbf{z}_F^l \in \mathbb{R}^{2X^l}$, the weight value corresponding to each modality can be inferred through fully connected (FC) operation and sigmoid mapping as follows:

$$\left[\omega_T^l, \omega_S^l\right] = \gamma\left(\mathbf{W}^l \mathbf{z}_F^l + \mathbf{b}^l\right). \tag{10}$$

Here, $\mathbf{W}^l$ and $\mathbf{b}^l$ represent the trainable weight and bias of the FC operation, respectively, and $\gamma(\cdot)$ refers to the sigmoid activation function [59]. Finally, ω_T^l and ω_S^l are normalized to obtain the fusion ratio for the target (i.e., $\alpha_T^l = \omega_T^l/(\omega_T^l + \omega_S^l)$) and shadow (i.e., $\alpha_S^l = \omega_S^l/(\omega_T^l + \omega_S^l)$).

In particular, we do not confine the application of the DFM to a specific layer; instead, we allow it to be leveraged across multiple encoding layers such that the network can

Algorithm 2 Inference Algorithm of the Proposed SAR IFTS Framework

Input:
test SAR sample $I[m, n]$,
depression angle for training ε_{train} and test ε_{test},
trained network $f_F(\cdot\,; \theta_T^*, \theta_S^*, \theta_F^*)$.

Step one: Image segmentation & preprocessing

Compute $I_v[m, n]$ by (3).
Segment the target $T[p, q]$ and shadow $S[p, q]$ from $I_v[m, n]$ as in Section III-A.
Compute $T_c[p', q']$ and $S_c[p', q']$ by (4). ▷ *Region-wise rescaling*
Compute $T_n[p', q']$ by (6). ▷ *Normalization*
Compute $S_n[p', q']$ by (7). ▷ *Inv. normalization*
return $T_n[p', q']$ and $S_n[p', q']$.

Step two: Network-based inference

$P(\tilde{y} \mid T_n, S_n) = f_F(T_n, S_n\,; \theta_T^*, \theta_S^*, \theta_F^*)$. ▷ *Parallel encoding*
$\tilde{Y} = \text{argmax}_Y\, P(\tilde{y} = Y \mid T_n, S_n)$.
return recognized output $\tilde{Y}$.

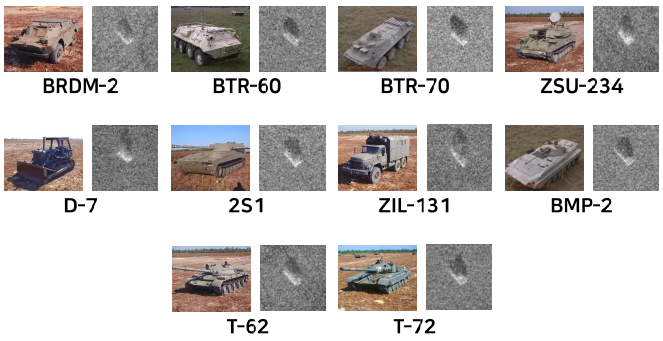

Fig. 9. Optical (left) and SAR (right) images for ten different ground vehicles.

further benefit from the effect of adaptive fusion. During the parallel encoding of the target and shadow, we allocate the DFM-driven adaptive weights for each layer where the region-wise features become resampled via the pooling operation, expressed as follows:

$$\eta_T^l \leftarrow \alpha_T^l \eta_T^l \quad \forall l \in \mathbb{L} \tag{11}$$

$$\eta_S^l \leftarrow \alpha_S^l \eta_S^l \quad \forall l \in \mathbb{L} \tag{12}$$

where $\mathbb{L}$ represents the set of the layers right after pooling operations in f. Now that the adaptive weights for the target and shadow regions are guaranteed across multiple layers, ATR can be performed by concatenating the final latent $\alpha_T^L \eta_T^L$ and $\alpha_S^L \eta_S^L$ from each subnetwork, followed by the application of the FC layers and softmax classifier to the fused feature vector.

To train the overall IFTS network $f_F(\cdot\ ; \theta_T, \theta_S, \theta_F)$, θ_T in the target-centric subnetwork $f_T(\cdot\ ; \theta_T)$, θ_S in the shadow-centric subnetwork $f_S(\cdot\ ; \theta_S)$, and the parameters θ_F corresponding to multistage DFMs must be considered comprehensively; all of them can be optimized in an end-to-end manner. The detailed learning and inference algorithms of the proposed IFTS framework are shown in Algorithms 1 and 2, respectively.

IV. Experimental Results

A. Dataset Description

To evaluate the proposed SAR-IFTS framework, we used the public MSTAR dataset [52] as a benchmark, which was established under the joint support of the Defense Advanced Research Projects Agency (DARPA) and the Air Force Research Laboratory (AFRL). The collection was based on the Sandia National Laboratory SAR sensor platform for ten different categories of ground military vehicles (armored personnel carrier: BMP-2, BRDM-2, BTR-60, and BTR-70; tank: T-62, T-72; air defense unit: ZSU-234; bulldozer: D-7; rocket launcher: 2S1; and truck: ZIL-131), which are shown in Fig. 9. For each category, the resulting SAR images were acquired from a full aspect coverage (i.e., from 0° to 360° azimuth angle varying at an interval of 5° to 6°) with a spatial resolution of 0.3 m × 0.3 m and a size of 128 × 128 pixels.

For a comprehensive evaluation of various scattering scenarios, the MSTAR dataset can mainly be divided into two setups depending on the operating conditions: the SOC and EOC. The SOC is defined as a ten-class SAR classification problem for ground objects measured from exactly the same target configurations and serial numbers, as well as at similar depression angles, reflecting almost ideal scenarios. The EOC setups are designed to assess the performance under more practical scattering conditions than the SOC and can further be categorized into three different variants, i.e., EOC-1, EOC-2, and EOC-3, each of which reflects the scenario of significant depression angle change, target configuration variance, and version variance, respectively. Detailed target information and the number of available SAR templates in each dataset setup are listed in Tables II–V.

To segment the target and shadow regions from a specified MSTAR SAR chip (see Section III-A), we utilized a 5 × 5 counting filter with a threshold of 15 and a 5 × 5 morphological image mask with its vertex pixels set to 0 as follows:

$$\begin{bmatrix} 0 & 1 & 1 & 1 & 0 \\ 1 & 1 & 1 & 1 & 1 \\ 1 & 1 & 1 & 1 & 1 \\ 1 & 1 & 1 & 1 & 1 \\ 0 & 1 & 1 & 1 & 0 \end{bmatrix}.$$

The final segmented size of each region, i.e., (P, Q), was set to $(96, 96)$.

B. Experimental Setup

Note that the proposed IFTS framework is generic, so it can be easily combined with other classification models regardless of the network topology. Hence, we comprehensively investigated the ATR performance based on various network structures, including backbone models specialized for SAR imagery, such as AConvNet [3], LM-BN-CNN [38], and ESENet [39], as well as baseline models developed in the image classification field, such as AlexNet [23], VGGNet [62], and ResNet [63]. By adding a global average pooling layer [63] to the last encoding layer (i.e., the layer right before the FC layers) and modifying the channel size of the input convolutional kernel to 1, each network was adjusted

TABLE II
TRAINING AND TEST SAR SAMPLES UNDER SOC EXPERIMENTAL SETUP

Class	Serial No.	Training		Test	
		Depression	Number	Depression	Number
BRDM-2	E-71	17°	298	15°	274
BTR-60	7532	17°	256	15°	195
BTR-70	C71	17°	233	15°	196
T-62	A51	17°	299	15°	273
ZSU-234	d08	17°	299	15°	274
D-7	13015	17°	299	15°	274
2S1	B01	17°	299	15°	274
ZIL-131	E12	17°	299	15°	274
BMP-2	9563	17°	233	15°	195
	9566	17°	232	15°	196
	C21	17°	233	15°	196
T-72	132	17°	232	15°	196
	812	17°	231	15°	195
	S7	17°	228	15°	191

TABLE III
TRAINING AND TEST SAR SAMPLES UNDER EOC-1 EXPERIMENTAL SETUP

Class	Serial No.	Training		Test	
		Depression	Number	Depression	Number
BRDM-2	E-71	17°	298	30°	287
ZSU-234	d08	17°	299	30°	288
2S1	B01	17°	299	30°	288
T-72	132	17°	232	-	-
	812	17°	231	-	-
	S7	17°	228	-	-
	A64	-	-	30°	288

TABLE IV
TRAINING AND TEST SAR SAMPLES UNDER EOC-2 EXPERIMENTAL SETUP

Class	Serial No.	Training		Test Variants	
		Depression	Number	Depression	Number
BRDM-2	E-71	17°	298	-	-
BTR-70	C71	17°	233	-	-
BMP-2	9563	17°	233	-	-
T-72	132	17°	232	-	-
	S7	-	-	15°, 17°	419
	A32	-	-	15°, 17°	572
	A62	-	-	15°, 17°	573
	A63	-	-	15°, 17°	573
	A64	-	-	15°, 17°	573

appropriately to manage the SAR images of an arbitrary input size.

Each model was trained for 300 epochs using the adaptive moment estimation (Adam) optimizer [64] at a learning rate of 0.001 and a batch size of 128. All the experiments were implemented based on the framework of Pytorch 1.6, which was executed on an Intel i7-9800K CPU with an Nvidia Titan RTX GPU (24 GB memory) and 64 GB of RAM.

TABLE V
TRAINING AND TEST SAR SAMPLES UNDER EOC-3 EXPERIMENTAL SETUP

Class	Serial No.	Training		Test Variants	
		Depression	Number	Depression	Number
BRDM-2	E-71	17°	298	-	-
BTR-70	C71	17°	233	-	-
BMP-2	9563	17°	233	-	-
	9566	-	-	15°, 17°	428
	C21	-	-	15°, 17°	429
T-72	132	17°	232	-	-
	812	-	-	15°, 17°	426
	A04	-	-	15°, 17°	573
	A05	-	-	15°, 17°	573
	A07	-	-	15°, 17°	573
	A10	-	-	15°, 17°	567

TABLE VI
EXPERIMENTAL RESULTS UNDER SOC SETUP

Speciality	Backbone	# Params	Accuracy [%]
Target Only (SAR)	AConvNet [3]	117K	95.12
	LM-BN-CNN [38]	141K	96.30
	ESENet [39]	555K	96.69
Target Only (Optical Image)	AlexNet [23]	57M	94.83
	VGGNet16 [62]	134M	94.67
	VGGNet19 [62]	140M	94.23
	ResNet18 [63]	11M	96.87
	ResNet34 [63]	21M	96.72
	ResNet50 [63]	24M	96.61
Target + Shadow	AConvNet + IFTS	235K	97.59 (+**2.47**)
	ESENet + IFTS	1.1M	*98.45* (+**1.76**)
	ResNet18 + IFTS	22M	**98.90** (+**2.03**)

C. Results Under SOC

As listed in Table II, the training and test datasets in the SOC setup comprise ten-class SAR images of the same target configurations and serial numbers captured from similar depression angles of 17° and 15°, respectively. Under this ideal setup, we measured the ATR accuracy of each baseline network by applying/not applying the proposed IFTS framework. Namely, one is based only on the target regions, similar to current SAR-ATR approaches [17], [38], [39], [65], whereas the other utilizes the target and shadow simultaneously through our IFTS-based encoding. Results are reported as the averages of five independent trials for statistical reliability.

The ATR results for each model are summarized in Table VI. In the table, we emphasize the best performance by the bold-face font and the second-best performance by the italic font. To provide a clearer comparison of the results, we also present the ATR performance with respect to the parameter size of each backbone model, as shown in Fig. 10. By comparing the outcomes of conventional target-only

TABLE VII
ATR RESULTS OF RESNET18 + IFTS IN CONFUSION MATRIX FORM UNDER THE SOC SETUP

Class	BRDM-2	BTR-60	BTR-70	T-62	ZSU-234	D-7	2S1	ZIL-131	BMP-2	T-72	Accuracy [%]
BRDM-2	268	3	1	0	0	0	0	1	1	0	97.81
BTR-60	5	189	0	0	1	0	0	0	0	0	96.92
BTR-70	0	0	194	0	0	0	2	0	0	0	98.98
T-62	0	0	0	269	1	0	0	1	0	2	98.53
ZSU-234	0	0	0	0	271	2	0	0	0	1	98.91
D-7	0	0	0	0	2	272	0	0	0	0	99.27
2S1	0	0	1	0	0	0	270	3	0	0	98.54
ZIL-131	0	0	0	0	3	0	0	270	0	1	98.54
BMP-2	0	1	0	0	0	0	0	0	583	3	99.32
T-72	0	0	0	1	0	0	0	0	0	581	99.83
Total											**98.88**

encodings (top nine rows of Table VI), it is noticeable that the ATR techniques customized for SAR imagery [3], [38], [39] exhibit satisfactory performance even with small numbers of training parameters. By contrast, the backbone models specialized in optical data pursue deeper layers and larger parameter sizes to further improve the representation capability of the extracted features, thereby resulting in ResNet18 achieving the best ATR accuracy among the existing techniques. Meanwhile, the oversized network inevitably requires more training SAR data to prevent overfitting and, consequently, indicates rather deteriorated performance over a certain number of training parameters. This demonstrates the fundamental limitations of current SAR-ATR approaches that attempt to improve the performance through changes in the model backbone since data acquisition is substantially laborious and expensive, particularly in SAR-based tasks.

Notably, applying the proposed IFTS framework allows all models to successfully exploit shadow modality and, hence, outperform each backbone counterpart to a large extent (the accuracy gain compared with its corresponding counterpart is also presented in the table). When coupled with the IFTS, even AConvNet can achieve an ATR performance superior to that of the previous best model based on target-only encoding, i.e., ResNet18 + target-only encoding, using significantly fewer training parameters (approximately 47 times lower than that of ResNet18). ResNet18 coupled with the IFTS demonstrates state-of-the-art performance under the SOC setup, 2.03% higher than its counterpart. These results support our motivation to exploit shadow information together for improved ATR. Detailed ATR results for ResNet18 + IFTS are shown in Table VII in a confusion matrix format.

Meanwhile, in terms of model parameters, the proposed IFTS framework includes variable model parameters with respect to its backbone network model, as shown in the third column of Table VI. That is, applying the IFTS framework additionally involves the encoding branch for shadow and the fusion branch composed of DFMs, thereby increasing the model parameter complexity by about twice that of the original backbone model. Nevertheless, the proposed IFTS framework is far superior to the conventional methods in terms of ATR performance with respect to the model complexity, as clearly shown in Fig. 10.

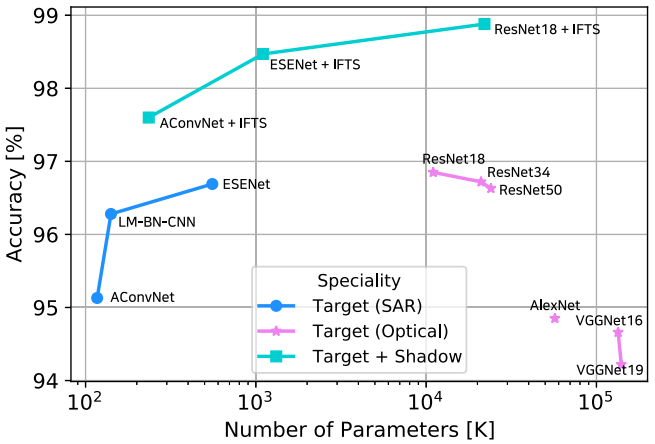

Fig. 10. SAR-ATR accuracy of various backbone models when trained with or without our IFTS framework under the SOC setup.

It should be noted that this study focused on the practicality and realization of the IFTS in the pattern analysis of radar imagery, i.e., we did not address detailed orthogonal factors that can further improve ATR performance, such as advanced segmentation algorithms of SAR imagery [66], [67], domain adaptation [31]–[33], and modern network architectures [34]–[36], [68]. We believe that combining such factors with the proposed IFTS framework will further improve robustness and generality.

D. Results Under EOCs

In this subsection, the numerical performance of each ATR model is investigated under different EOC setups, which reflects more practical circumstances than the SOC setup. The overall results for the EOC-1, EOC-2, and EOC-3 datasets are organized in Table VIII.

1) Results Under EOC-1: The EOC-1 setup corresponds to the scenario of significant depression angle changes and comprises four-class training and test data obtained from depression angles of 17° and 30°, respectively (see Table III).

TABLE VIII
EXPERIMENTAL RESULTS UNDER EOC SETUPS

Speciality	Backbone	# Params	Accuracy [%]		
			under EOC-1	under EOC-2	under EOC-3
Target Only (SAR)	AConvNet [3]	110K	91.83	88.23	87.25
	LM-BN-CNN [38]	141K	93.41	88.96	88.12
	ESENet [39]	555K	93.57	89.81	89.33
Target Only (Optical Image)	AlexNet [23]	57M	91.05	87.68	86.55
	VGGNet16 [62]	134M	89.94	87.27	86.63
	VGGNet19 [62]	140M	90.10	87.04	86.47
	ResNet18 [63]	11M	93.75	90.21	90.31
	ResNet34 [63]	21M	93.92	90.63	89.97
	ResNet50 [63]	24M	93.66	90.44	89.83
Target + Shadow	AConvNet + IFTS	222K	95.04 (+**3.21**)	97.23 (+**9.00**)	94.48 (+**7.23**)
	ESENet + IFTS	1.1M	*95.83* (+**2.26**)	*97.90* (+**8.09**)	*95.09* (+**5.76**)
	ResNet18 + IFTS	22M	**96.86** (+**3.11**)	**98.28** (+**8.07**)	**95.46** (+**5.15**)

TABLE IX
ATR RESULTS OF RESNET18 + IFTS IN CONFUSION MATRIX FORM UNDER EOC-1 SETUP

Class	BRDM-2	ZSU-234	2S1	T-72	Accuracy [%]
BRDM-2	284	1	2	0	98.95
ZSU-234	0	282	2	4	98.26
2S1	7	0	277	4	96.18
T-72	6	7	3	272	94.44
Total					**96.87**

TABLE X
ATR RESULTS OF RESNET18 + IFTS IN CONFUSION MATRIX FORM UNDER EOC-2 SETUP

Class	Serial No.	BRDM-2	BTR-70	BMP-2	T-72	Accuracy [%]
T-72	S7	0	0	10	409	97.61
	A32	1	1	2	568	99.30
	A62	0	2	5	566	98.78
	A63	6	0	10	557	97.21
	A64	0	4	7	562	98.08
Total						**98.23**

Based on the first column of Table VIII, which shows the results for EOC-1, it can be observed that the overall ATR performance deteriorates compared with the SOC setup, despite the decrease in the number of classes to be categorized (i.e., from ten to four classes). This indicates the difficulty in capturing an appropriate high-level representation under significant depression angle differences between the training and test SAR data. Fortunately, it is remarkable that applying the proposed IFTS framework can increase ATR accuracies with larger margins compared with SOC setup across all counterpart backbones: improvements by 3.21% for AConvNet, 2.26% for ESENet, and 3.11% for ResNet18. Detailed EOC-1 results of the ResNet18 backbone model combined with the IFTS are presented in Table IX in a confusion matrix format.

2) Results Under EOC-2: EOC-2 is a four-class classification setup for evaluating ATR performance in a scenario where the target configuration varies between training and testing (see Table IV). The results under the EOC-2 setup (the second column of Table VIII) reveal that the conventional models with target-only encoding yield further degraded accuracies when the target configurations are varied compared with the EOC-1 case where the depression angles are varied. Nevertheless, when the proposed IFTS framework is applied, all networks indicate huge performance improvements (i.e., improvements by 9.00% for AConvNet, 8.09% for ESENet, and 8.07% for ResNet18), resulting in even higher accuracies compared to those under EOC-1. Therefore, we can infer that the shadow region can provide further complementary indicators in the scenario of configuration variant compared with the other setups. Table X shows the confusion matrix of the results of the ResNet18 backbone model with IFTS under the EOC-2 setup.

3) Results Under EOC-3: This setup reflects the scenario where the target versions are varied, and it comprises four-class training SAR data and two-class test data with versions different from those in training (see Table V). The results of the EOC-3 setup (the third column of Table VIII) show that the models based on IFTS encoding outperform those based on conventional target-only encoding by a large margin (i.e., improvements by 7.23% for AConvNet, 5.76% for ESENet, and 5.15% for ResNet18), demonstrating the effectiveness of the proposed IFTS framework even in the scenario involving different target versions between training and testing. The confusion matrix for the ResNet18 + IFTS model is presented in Table XI.

4) Overall Discussion of EOC Results: Overall, the ATR models in the EOC setups highly benefit from the proposed IFTS framework regardless of the backbone topology; they exhibit even greater accuracy improvements compared with the SOC setup. Considering the aforementioned concern that the ATR performance can rather be degraded when the shadow information is incautiously incorporated without compensation for its unique domain characteristics (as discussed in

TABLE XI
ATR RESULTS OF RESNET18 + IFTS IN CONFUSION MATRIX FORM UNDER EOC-3 SETUP

Class	Serial No.	BRDM-2	BTR-70	BMP-2	T-72	Accuracy [%]
BMP-2	9566	10	0	418	0	97.66
	C21	7	1	420	1	97.90
T-72	812	2	11	17	396	92.96
	A04	0	3	29	541	94.42
	A05	0	0	20	553	96.51
	A07	8	3	27	535	93.37
	A10	0	3	18	546	96.30
Total						**95.52**

Section II-B), these results not only support our motivation to enable the cooperative implementation of shadow-centric processing based on a parallelized mechanism but also validate the practicality of the proposed IFTS framework.

E. Ablation Study: Effectiveness of Shadow-Centric Preprocessing

To systematically explore the effects of the proposed shadow-centric processing techniques (i.e., image rescaling for shadow and inverse normalization), we herein report the performance of several ATR models trained with only shadow information. We compared three different combinations of shadow preprocessing pipelines under the SOC and EOC-1 setups while fixing the other conditions. The results for each setup are illustrated in Fig. 11.

As presented in Fig. 11(a), which corresponds to the results of the SOC, adding a shadow-oriented rescaling algorithm increases the ATR accuracy across all backbone models (a 0.59% increase on average) compared with conventional processing, and further improves the performance when combined with the inverse normalization technique (an additional increase of 3.74% on average). In addition, it can be observed that appropriate preprocessing is much more influential than network architectures in managing shadow regions. The relative effectiveness of the shadow-oriented rescaling compared with inverse normalization is due to the marginal difference in the depression angle between training and test under the ideal SOC condition. As shown by the results under significant depression angle differences [see Fig. 11(b)], it is clear that the shadow-oriented rescaling technique is extremely beneficial; it affords a significant improvement of 13.77% on average compared with the additional increase of 2.14% when inverse normalization is added. In general, the results above explicitly demonstrate the validity of the proposed preprocessing techniques for shadows, particularly under practical sensing scenarios.

F. Ablation Study: Effectiveness of Fusion Strategies

To validate the effect of the proposed fusion strategies (i.e., adaptive fusion using multistage DFMs) for disparate target and shadow information, we evaluate the ATR performance of the SOC dataset under several plausible fusion rules: 1) using the target area alone; 2) using both target and shadow regions in a single image (i.e., pixel-level fusion); 3) concatenation-based fusion of last-layer features; 4) DFM-based fusion of last-layer features; and 5) DFM-based fusion of multistage features.

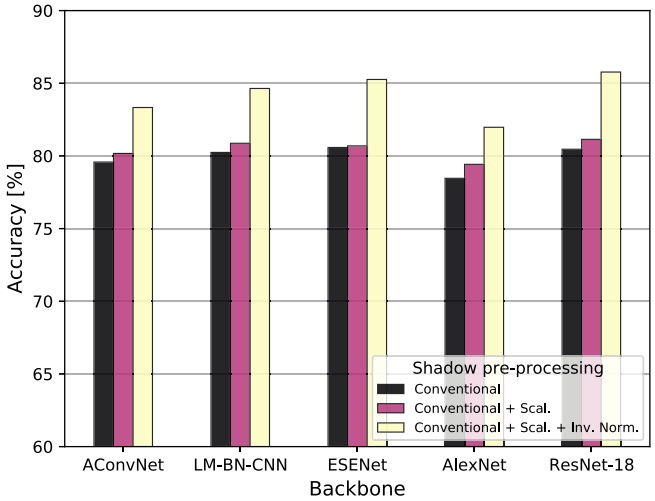

(a)

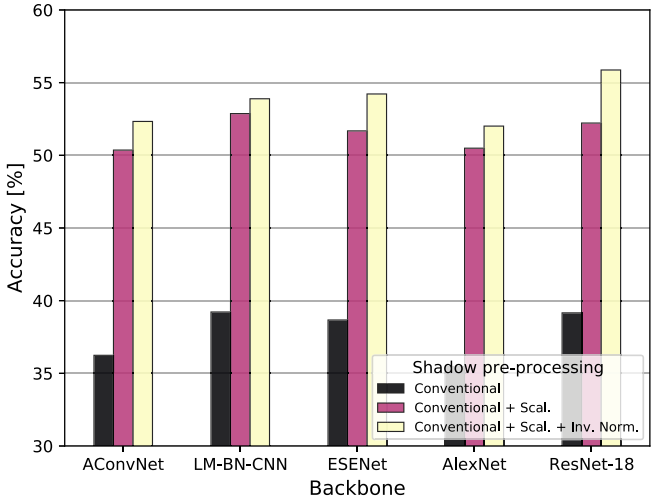

(b)

Fig. 11. SAR-ATR accuracy of various backbone models trained only on shadow modalities with different preprocessing. (a) Results under SOC setup. (b) Results under EOC-1 setup.

Fig. 12 summarizes the results under SOC and EOC-1 setups. The comparison between the target-only encoding and pixel-level fusion clearly demonstrates that the pixel-level fusion-based IFTS cannot benefit from the shadow region at all under the EOC-1 setup, meaning that leveraging target and shadow together in a single SAR image cannot properly address their disparate characteristics, particularly when the depression angle largely changes from the training condition. Meanwhile, the DFM-based fusion rules outperform the pixel-level and concatenation-based fusion rules significantly, which indicates the importance of the adaptive integration of target and shadow for SAR-ATR. In addition, our multilayer fusion strategy can further strengthen the representation

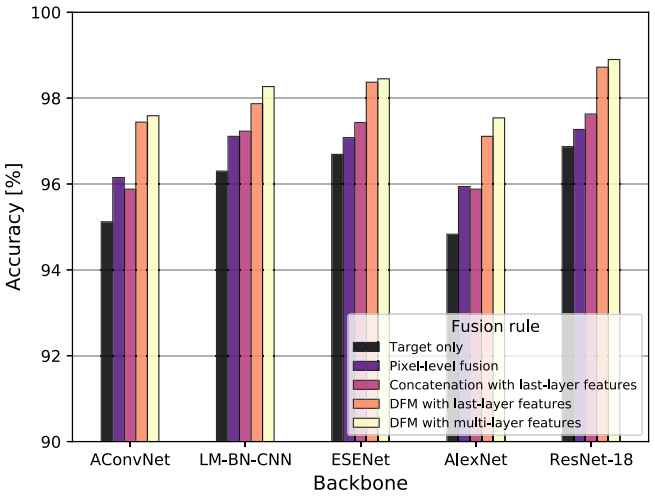

(a)

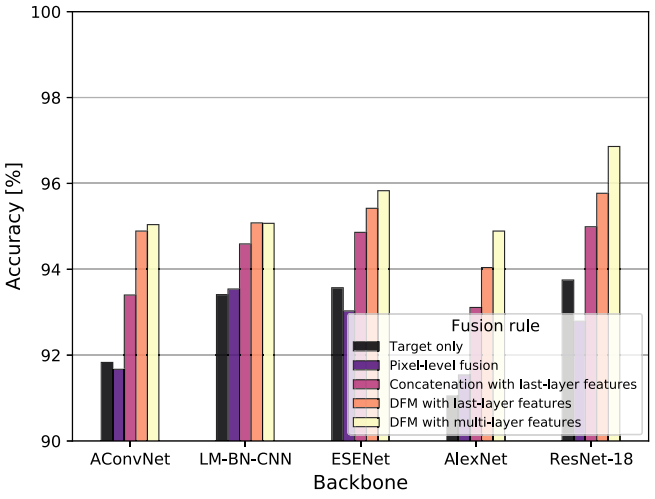

(b)

Fig. 12. SAR-ATR accuracy of various backbone models based on different fusion rules. (a) Results under the SOC setup. (b) Results under the EOC-1 setup.

capability of each network, leading to a further increment in ATR accuracy in comparison with last-layer fusion.

G. Ablation Study: Qualitative Analysis in DFM Weights

We perform an additional ablation study to validate whether the discriminative features of shadow work in a complementary manner with the target region under our proposed pipeline. From the trained ResNet18 network coupled with our IFTS scheme, we observe the changes of target and shadow weights (i.e., α_T and α_S) within the proposed DFMs, with respect to several test SAR samples. Fig. 13 illustrates the test SAR samples under SOC and EOC-1 environments, and the corresponding weight values for target and shadow. When the target area in SAR includes sufficient cues for the object of interest (first, second, fourth, and fifth columns of Fig. 13), the DFMs tend to assign strong weight to the target reflection. In contrast, in some unusual samples where the target area cannot offer sufficient cue for ATR, while the

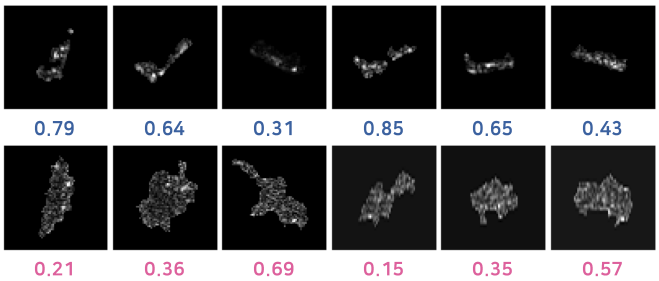

Fig. 13. Average DFM weights for target and shadow with respect to several test SAR samples. The left three samples are under SOC, and the remaining right three samples are under EOC-1.

shadow area rather contains discriminative semantics (third and sixth columns of Fig. 13), the shadow weights significantly increase compared to the target, indicating that the DFM can stimulate the network to leverage the shadow's complementary information for improved ATR.

V. Conclusion

Shadow signature in SAR imagery includes backscattered components of an object's configuration, as with direct target reflections. However, its unique domain properties, which are distinct from the target region, result in substantial incompatibility with the target, rendering shadows inoperative in current SAR-ATR tasks. To induce a network such that the benefit from the joint utilization of the target and shadow can be reaped effectively, we proposed an IFTS framework comprising novel solutions in three aspects. First, we designed a new series of preprocessing techniques specifically customized for the shadow region to compensate for its contradictory nature compared with the target. Second, we presented a parallelized SAR encoding pipeline such that independent processing for the target and shadow can be guaranteed structurally, thereby resulting in a representation pair oriented toward each modality. Third, we proposed a multistage fusion strategy based on DFMs, which enabled an adaptive fusion of the target and shadow while accounting for their relative significance. Based on extensive experiments using a public SAR benchmark dataset, we observed that our IFTS successfully enabled a network to improve its understanding of the shadow region, thereby achieving state-of-the-art performances under ideal SOC and practical EOC setups.

References

[1] M. Soumekh, *Synthetic Aperture Radar Signal Processing*. New York, NY, USA: Wiley, 1999.

[2] M. Kirscht *et al.*, "An airborne radar sensor for maritime and ground surveillance and reconnaissance—Algorithmic issues and exemplary results," *IEEE J. Sel. Topics Appl. Earth Observ. Remote Sens.*, vol. 9, no. 3, pp. 971–979, Mar. 2016.

[3] S. Chen, H. Wang, F. Xu, and Y.-Q. Jin, "Target classification using the deep convolutional networks for SAR images," *IEEE Trans. Geosci. Remote Sens.*, vol. 54, no. 8, pp. 4806–4817, Apr. 2016.

[4] C. Wang, M. Zhang, Z.-W. Xu, C. Chun, and D.-S. Sheng, "Effects of anisotropic ionospheric irregularities on space-borne SAR imaging," *IEEE Trans. Antennas Propag.*, vol. 62, no. 9, pp. 4664–4673, Sep. 2014.

[5] A. Fiche, S. Angelliaume, L. Rosenberg, and A. Khenchaf, "Analysis of X-band SAR sea-clutter distributions at different grazing angles," *IEEE Trans. Geosci. Remote Sens.*, vol. 53, no. 8, pp. 4650–4660, Aug. 2015.

[6] B. Zhao, L. Huang, J. Li, and P. Zhang, "Target reconstruction from deceptively jammed single-channel SAR," *IEEE Trans. Geosci. Remote Sens.*, vol. 56, no. 1, pp. 152–167, Jan. 2018.

[7] R. C. P. Marques, F. N. Medeiros, and J. S. Nobre, "SAR image segmentation based on level set approach and G_A^0 model," *IEEE Trans. Pattern Anal. Mach. Intell.*, vol. 34, no. 10, pp. 2046–2057, Oct. 2012.

[8] V. S. Frost, J. A. Stiles, K. S. Shanmugan, and J. C. Holtzman, "A model for radar images and its application to adaptive digital filtering of multiplicative noise," *IEEE Trans. Pattern Anal. Mach. Intell.*, vol. PAMI-4, no. 2, pp. 157–166, Mar. 1982.

[9] D. E. Dudgeon and R. T. Lacoss, "An overview of automatic target recognition," *Lincoln Lab. J.*, vol. 6, no. 1, pp. 3–10, 1993.

[10] L. M. Novak, G. J. Owirka, W. S. Brower, and A. L. Weaver, "The automatic target-recognition system in SAIP," *Lincoln Lab. J.*, vol. 10, no. 2, pp. 1–16, 1997.

[11] Q. Zhao and J. C. Principe, "Support vector machines for SAR automatic target recognition," *IEEE Trans. Aerosp. Electron. Syst.*, vol. 37, no. 2, pp. 643–654, Apr. 2001.

[12] G. Jones and B. Bhanu, "Recognition of articulated and occluded objects," *IEEE Trans. Pattern Anal. Mach. Intell.*, vol. 21, no. 7, pp. 603–613, Jul. 1999.

[13] Z. Jianxiong, S. Zhiguang, C. Xiao, and F. Qiang, "Automatic target recognition of SAR images based on global scattering center model," *IEEE Trans. Geosci. Remote Sens.*, vol. 49, no. 10, pp. 3713–3729, Oct. 2011.

[14] C. Enderli, L. Savy, and P. Refregier, "Application of the deflection criterion to classification of radar SAR images," *IEEE Trans. Pattern Anal. Mach. Intell.*, vol. 29, no. 9, pp. 1668–1672, Sep. 2007.

[15] U. Srinivas, V. Monga, and R. G. Raj, "SAR automatic target recognition using discriminative graphical models," *IEEE Trans. Aerosp. Electron. Syst.*, vol. 50, no. 1, pp. 591–606, Jan. 2014.

[16] J.-I. Park and K.-T. Kim, "Modified polar mapping classifier for SAR automatic target recognition," *IEEE Trans. Aerosp. Electron. Syst.*, vol. 50, no. 2, pp. 1092–1107, Apr. 2014.

[17] B. Ding, G. Wen, C. Ma, and X. Yang, "An efficient and robust framework for SAR target recognition by hierarchically fusing global and local features," *IEEE Trans. Image Process.*, vol. 27, no. 12, pp. 5983–5995, Dec. 2018.

[18] G. Dong, N. Wang, and G. Kuang, "Sparse representation of monogenic signal: With application to target recognition in SAR images," *IEEE Signal Process. Lett.*, vol. 21, no. 8, pp. 952–956, Aug. 2014.

[19] O. Kechagias-Stamatis and N. Aouf, "Fusing deep learning and sparse coding for SAR ATR," *IEEE Trans. Aerosp. Electron. Syst.*, vol. 55, no. 2, pp. 785–797, Apr. 2019.

[20] P. P. Gandhi and S. A. Kassam, "Analysis of CFAR processors in nonhomogeneous background," *IEEE Trans. Aerosp. Electron. Syst.*, vol. AES-24, no. 4, pp. 427–445, Jul. 1988.

[21] Y. Chen, E. Blasch, T. Qian, and E. Blasch, "Experimental feature-based SAR ATR performance evaluation under different operational conditions," *Proc. SPIE*, vol. 6968, May 2008, Art. no. 69680F.

[22] A. Jain and D. Zongker, "Feature selection: Evaluation, application, and small sample performance," *IEEE Trans. Pattern Anal. Mach. Intell.*, vol. 19, no. 2, pp. 153–158, Feb. 1997.

[23] A. Krizhevsky, I. Sutskever, and G. E. Hinton, "ImageNet classification with deep convolutional neural networks," in *Proc. Adv. Neural Inf. Process. Syst. (NIPS)*, vol. 25. Stateline, NV, USA, Dec. 2012, pp. 1097–1105.

[24] M. Tan, R. Pang, and Q. V. Le, "EfficientDet: Scalable and efficient object detection," in *Proc. IEEE/CVF Conf. Comput. Vis. Pattern Recognit. (CVPR)*, Jun. 2020, pp. 10778–10787.

[25] H. Purwins, B. Li, T. Virtanen, J. Schlüter, S.-Y. Chang, and T. Sainath, "Deep learning for audio signal processing," *IEEE J. Sel. Topics Signal Process.*, vol. 13, no. 2, pp. 206–219, Apr. 2019.

[26] B. Yang, R. Guo, M. Liang, S. Casas, and R. Urtasun, "RadarNet: Exploiting radar for robust perception of dynamic objects," in *Proc. Eur. Conf. Comput. Vis.*, Glasgow, U.K., Aug. 2020, pp. 496–512.

[27] S. A. Wagner, "SAR ATR by a combination of convolutional neural network and support vector machines," *IEEE Trans. Aerosp. Electron. Syst.*, vol. 52, no. 6, pp. 2861–2872, Dec. 2016.

[28] J. Ding, B. Chen, H. Liu, and M. Huang, "Convolutional neural network with data augmentation for SAR target recognition," *IEEE Geosci. Remote Sens. Lett.*, vol. 13, no. 3, pp. 364–368, Mar. 2016.

[29] Z. Cui, M. Zhang, Z. Cao, and C. Cao, "Image data augmentation for SAR sensor via generative adversarial nets," *IEEE Access*, vol. 7, pp. 42255–42268, 2019.

[30] C. Zheng, X. Jiang, and X. Liu, "Semi-supervised SAR ATR via multi-discriminator generative adversarial network," *IEEE Sensors J.*, vol. 19, no. 17, pp. 7525–7533, Sep. 2019.

[31] K. Wang, G. Zhang, and H. Leung, "SAR target recognition based on cross-domain and cross-task transfer learning," *IEEE Access*, vol. 7, pp. 153391–153399, 2019.

[32] Z. Huang, Z. Pan, and B. Lei, "What, where, and how to transfer in SAR target recognition based on deep CNNs," *IEEE Trans. Geosci. Remote Sens.*, vol. 58, no. 4, pp. 2324–2336, Apr. 2020.

[33] F. Ye, W. Luo, M. Dong, H. He, and W. Min, "SAR image retrieval based on unsupervised domain adaptation and clustering," *IEEE Geosci. Remote Sens. Lett.*, vol. 16, no. 9, pp. 1482–1486, Sep. 2019.

[34] J. Pei, Y. Huang, Z. Sun, Y. Zhang, J. Yang, and T.-S. Yeo, "Multiview synthetic aperture radar automatic target recognition optimization: Modeling and implementation," *IEEE Trans. Geosci. Remote Sens.*, vol. 56, no. 11, pp. 6425–6439, Nov. 2018.

[35] X. Bai, R. Xue, L. Wang, and F. Zhou, "Sequence SAR image classification based on bidirectional convolution-recurrent network," *IEEE Trans. Geosci. Remote Sens.*, vol. 57, no. 11, pp. 9223–9235, Nov. 2019.

[36] R. Xue, X. Bai, and F. Zhou, "Spatial–temporal ensemble convolution for sequence SAR target classification," *IEEE Trans. Geosci. Remote Sens.*, vol. 59, no. 2, pp. 1250–1262, Feb. 2021.

[37] Z. Zhang, H. Wang, F. Xu, and Y.-Q. Jin, "Complex-valued convolutional neural network and its application in polarimetric SAR image classification," *IEEE Trans. Geosci. Remote Sens.*, vol. 55, no. 12, pp. 7177–7188, Dec. 2017.

[38] F. Zhou, L. Wang, X. Bai, and Y. Hui, "SAR ATR of ground vehicles based on LM-BN-CNN," *IEEE Trans. Geosci. Remote. Sens.*, vol. 56, no. 12, pp. 7282–7293, Dec. 2018.

[39] L. Wang, X. Bai, and F. Zhou, "SAR ATR of ground vehicles based on ESENet," *Remote Sens.*, vol. 11, no. 11, pp. 1–16, Jun. 2019.

[40] A. Filippidis, L. C. Jain, and N. Martin, "Fusion of intelligent agents for the detection of aircraft in SAR images," *IEEE Trans. Pattern Anal. Mach. Intell.*, vol. 22, no. 4, pp. 378–384, Apr. 2000.

[41] R. Schumacher and J. Schiller, "Non-cooperative target identification of battlefield targets–classification results based on SAR images," in *Proc. IEEE Int. Radar Conf.*, May 2005, pp. 167–172.

[42] S.-H. Kim, W.-J. Song, and S.-H. Kim, "Robust ground target detection by SAR and IR sensor fusion using Adaboost-based feature selection," *Sensors*, vol. 16, no. 7, pp. 1–27, Jul. 2016.

[43] A. W. Doerry, "Comments on airborne ISR radar utilization," *Proc. SPIE*, vol. 9829, pp. 504–515, May 2016.

[44] A. M. Raynal, D. L. Bickel, and A. W. Doerry, "Stationary and moving target shadow characteristics in synthetic aperture radar," *Proc. SPIE*, vol. 9077, pp. 413–427, May 2014.

[45] S. Papson and R. M. Narayanan, "Classification via the shadow region in SAR imagery," *IEEE Trans. Aerosp. Electron. Syst.*, vol. 48, no. 2, pp. 969–980, Apr. 2012.

[46] M. Jahangir, D. Blacknell, C. P. Moate, and R. D. Hill, "Extracting information from shadows in SAR imagery," in *Proc. Int. Conf. Mach. Vis.*, Dec. 2007, pp. 107–112.

[47] K. Tang, X. Sun, H. Sun, and H. Wang, "A geometrical-based simulator for target recognition in high-resolution SAR images," *IEEE Geosci. Remote Sens. Lett.*, vol. 9, no. 5, pp. 958–962, Sep. 2012.

[48] P. Lombardo, M. Sciotti, and L. M. Kaplan, "SAR prescreening using both target and shadow information," in *Proc. IEEE Radar Conf.*, May 2001, pp. 147–152.

[49] J. Cui, J. Gudnason, and M. Brookes, "Radar shadow and superresolution features for automatic recognition of MSTAR targets," in *Proc. IEEE Int. Radar Conf.*, May 2005, pp. 534–539.

[50] F. Gao, J. You, J. Wang, J. Sun, E. Yang, and H. Zhou, "A novel target detection method for SAR images based on shadow proposal and saliency analysis," *Neurocomputing*, vol. 267, pp. 220–231, Dec. 2017.

[51] C. Belloni, A. Balleri, N. Aouf, J.-M. Le Caillec, and T. Merlet, "Explainability of deep SAR ATR through feature analysis," *IEEE Trans. Aerosp. Electron. Syst.*, vol. 57, no. 1, pp. 659–673, Feb. 2021.

[52] E. Keydel, S. Lee, and J. Moore, "MSTAR extended operating conditions: A tutorial," *Proc. SPIE*, vol. 2757, pp. 228–242, Jun. 1996.

[53] C. Feichtenhofer, H. Fan, J. Malik, and K. He, "Slowfast networks for video recognition," in *Proc. IEEE/CVF Int. Conf. Comput. Vis. (ICCV)*, Oct. 2019, pp. 6201–6210.

[54] Y.-G. Jiang, Z. Wu, J. Wang, X. Xue, and S.-F. Chang, "Exploiting feature and class relationships in video categorization with regularized deep neural networks," *IEEE Trans. Pattern Anal. Mach. Intell.*, vol. 40, no. 2, pp. 352–364, Feb. 2018.

[55] W. G. Kropatsch and D. Strobl, "The generation of SAR layover and shadow maps from digital elevation models," *IEEE Trans. Geosci. Remote Sens.*, vol. 28, no. 1, pp. 98–107, Jan. 1990.
[56] J. Ngiam, A. Khosla, M. Kim, J. Nam, H. Lee, and A. Ng, "Multimodal deep learning," in *Proc. IMLS*, Jul. 2011, pp. 689–696.
[57] R. Meth, "Target/shadow segmentation and aspect estimation in synthetic aperture radar imagery," *Proc. SPIE*, vol. 3370, pp. 188–196, Sep. 1998.
[58] M. Chang and X. You, "Target recognition in SAR images based on information-decoupled representation," *Remote Sens.*, vol. 10, no. 1, pp. 1–19, Jan. 2018.
[59] I. Goodfellow, Y. Bengio, and A. Courville, *Deep Learning*. Cambridge, MA, USA: MIT Press, 2016. [Online]. Available: http://www.deeplearningbook.org
[60] A. Vaswani *et al.*, "Attention is all you need," in *Proc. Adv. Neural Inf. Process. Syst.*, vol. 30. Long Beach, CA, USA, Dec. 2017, pp. 1–11.
[61] Q. Wang, B. Wu, P. Zhu, P. Li, W. Zuo, and Q. Hu, "ECA-Net: Efficient channel attention for deep convolutional neural networks," in *Proc. IEEE/CVF Conf. Comput. Vis. Pattern Recognit. (CVPR)*, Jun. 2020, pp. 11534–11542.
[62] K. Simonyan and A. Zisserman, "Very deep convolutional networks for large-scale image recognition," in *Proc. ICLR*, San Diego, CA, USA, May 2015, pp. 1–14.
[63] K. He, X. Zhang, S. Ren, and J. Sun, "Deep residual learning for image recognition," in *Proc. IEEE Conf. Comput. Vis. Pattern Recognit. (CVPR)*, Jun. 2016, pp. 770–778.
[64] D. P. Kingma and J. Ba, "Adam: A method for stochastic optimization," in *Proc. Int. Conf. Learn. Represent. (ICLR)*, San Diego, CA, USA, May 2015, pp. 1–15.
[65] H. Zhu, T. Wong, N. Lin, W. Wang, and S. Thedoridis, "Synthetic aperture radar target classification based on 3-D convolutional neural network," in *Proc. IEEE 5th Int. Conf. Signal Image Process. (ICSIP)*, Oct. 2020, pp. 440–445.
[66] D. Malmgren-Hansen and M. Nobel-Jørgensen, "Convolutional neural networks for SAR image segmentation," in *Proc. IEEE Int. Symp. Signal Process. Inf. Technol. (ISSPIT)*, Dec. 2015, pp. 231–236.
[67] M. Heiligers and A. Huizing, "On the importance of visual explanation and segmentation for SAR ATR using deep learning," in *Proc. IEEE Radar Conf. (RadarConf18)*, Apr. 2018, pp. 394–399.
[68] M. Tan and Q. Le, "EfficientNet: Rethinking model scaling for convolutional neural networks," in *Proc. Mach. Learn. Res.*, vol. 97, K. Chaudhuri and R. Salakhutdinov, Eds. Long Beach, CA, USA, Jun. 2019, pp. 6105–6114.

Jae-Ho Choi received the B.S. degree in computer science and communication engineering from Korea University, Seoul, South Korea, in 2017, and the M.S. degree in electrical engineering from the Pohang University of Science and Technology, Pohang, South Korea, in 2019, where he is pursuing the Ph.D. degree with the Intelligent Radar Signal Processing Laboratory.

His research interests include radar signal processing, radio-based IoT systems, machine learning, SAR detection/recognition, and sensor fusion.

Myung-Jun Lee received the B.S. degree in computer science and electrical engineering from Handong Global University, Pohang, South Korea, in 2014, and the M.S. and Ph.D. degrees in electrical engineering from the Pohang University of Science and Technology, Pohang, in 2017 and 2021, respectively.

Since 2021, he has been with the Korea Aerospace Research Institute, Daejeon, South Korea, as a Senior Researcher. His research interests include radar signal processing, satellite data service systems, and big-data systems.

Nam-Hoon Jeong received the B.S. and M.S. degrees in electrical engineering from the Pohang University of Science and Technology, Pohang, South Korea, in 2015 and 2018, respectively, where he is pursuing the Ph.D. degree with the Intelligent Radar Signal Processing Laboratory.

His research interests include radar signal processing, pattern recognition, SAR detection/recognition, and radar resource management.

Geon Lee received the B.S. degree in electronics engineering from Kyungpook National University, Daegu, South Korea, in 2019. He is pursuing the M.S. degree with the Intelligent Radar Signal Processing Laboratory, Pohang University of Science and Technology, Pohang, South Korea.

His research interests include radar signal processing and radar target detection.

Kyung-Tae Kim (Member, IEEE) received the B.S., M.S., and Ph.D. degrees in electrical engineering from the Pohang University of Science and Technology (POSTECH), Pohang, South Korea, in 1994, 1996, and 1999, respectively.

From 2002 to 2010, he was a Faculty Member with the Department of Electronic Engineering, Yeungnam University, Gyeongsan, South Korea. Since 2011, he has been with the Department of Electrical Engineering, POSTECH, where he is a Professor. From 2012 to 2017, he served as the Director of the Sensor Target Recognition Laboratory, sponsored by the Defense Acquisition Program Administration and the Agency for Defense Development. He is also the Director of the Unmanned Surveillance and Reconnaissance Technology Research Center and the Next Generation Imaging Radar System Research Center, POSTECH. He is carrying out several research projects funded by the Korean government and several industries. He has authored over 300 papers on journal articles and conference proceedings. His research interests are mainly in the field of intelligent radar systems and signal processing: SAR/ISAR imaging, target recognition, the direction of arrival estimation, micro-Doppler analysis, automotive radars, digital beamforming, electronic warfare, and electromagnetic scattering.

Prof. Kim is a member of the Korea Institute of Electromagnetic Engineering and Science (KIEES). He was a recipient of several outstanding research awards and best paper awards from KIEES and international conferences.